Advances in Nano Research, *Vol. 13, No.6 (2022) 527-543*
https://doi.org/10.12989/anr.2022.13.6.527

In-situ functionalized biomass derived graphite-supported $BiFeO_3$ for eradication of pollutants

Deepeka[1], Paramdeep Kaur[1], Jyoti[1], Sandeep Bansal[2] and Sonal Singhal*[1]

[1]*Department of Chemistry, Panjab University, Chandigarh, 160014, India*
[2]*Department of Science and Technology, New Delhi, India*

(*Received May 7, 2021, Revised August 26, 2022, Accepted September 14, 2022*)

Abstract. A novel, green, versatile and magnetically retrievable $BiFeO_3$/CDR (Bismuth ferrite/coriander) nanocomposites were fabricated via simple wet chemical method utilizing in situ functionalized, cheap coriander seed powder (CDR 5%, 10%, 15% and 20 wt%) as a fuel to enhance the efficiency of pristine $BiFeO_3$. A comparative study was performed between $BiFeO_3$/CDR and $BiFeO_3$/CNT (Bismuth ferrite/carbon nanotubes) nanocomposites for the removal of various hazardous pollutants from waste water. The successful synthesis of the fabricated nanomaterials was monitored via FT-IR, Powder XRD, FE-SEM, CV, VSM, CHNS/O and XPS studies. The synthesized nanomaterials were employed for the oxidative degradation of Carbol fuchsin, Reactive black 5, Ciprofloxacin and Doxorubicin; adsorption of a pesticide malathion; and reduction studies for Para-nitrophenol (PNP). The fabricated nanomaterials ($BiFeO_3$/CDR) showcased excellent efficiency and comparable results with ($BiFeO_3$/CNT) for the removal of model pollutants. Moreover, synthesized green heterojunction was also testified for mixture of textile and pharmaceutical waste. Hence CDR can be utilized as a better alternative of CNTs.

Keywords: adsorption; Bismuth ferrite; CNTs; eco-friendly alternative; graphite; oxidative degradation; reduction; water treatment

1. Introduction

Environmental pollution and shortage of clean water due to increasing emission of industrial effluents such as dyes, drugs and pesticides into the water bodies, pose a serious threat to health of living beings (Kaur *et al*. 2016, Shah and Rather 2021). Due to high chemical stability and complex structure, these effluents are resistant towards bio-degradation. Presence of even small amount of these effluents in water is extremely harmful attributable to their toxic, carcinogenic and mutagenic nature (Tsuboy *et al*. 2007, Girgis *et al*. 2015). Treatment and elimination of these pollutants from water is urgent for betterment of both aquatic and human life. Catalysis has become a promising field to meet the challenges faced by the present day world. Various catalysts such as nanocomposites $BiVO_4$ /N-rGO, metal oxides (Fe_2O_3, NiO, CuO and Fe_2O_4), zinc ferrite nanoparticles, Tin modified-TiO_2 powder, multifunctional $NiFe_2O_4$ /ZnO hybrids, semiconductors (ZnO, CdS, $BiFeO_3$ and TiO_2) (Kaur *et al*. 2019) (Soltani *et al*. 2013) have been reported to tackle these industrial disseminated pollutants.

Out of which, semiconductor nanomaterials having perovskite structure are receiving immense importance due to their low cost, higher thermal stability, low band gap (~2.05eV) (Gua *et al*. 2010). Amongst various semi-conductor materials bismuth ferrite (BFO), which is a multi-ferroic material, has been utilized extensively owing to good chemical stability, multi-ferroic properties and existence of its band gap in visible light region. Moreover, the magnetic nature of ferrite provides additional advantage during catalytic reaction; the catalyst can be easily recovered and reused using the external magnet. Unfortunately, use of pristine BFO is associated with few limitations such as low surface area and higher recombination rate of holes/electron pairs (Irfan *et al*. 2019, Gua *et al*. 2010). Therefore, modification of BFO in order to avoid its limitations seems reasonable solution. Utilization of carbon based materials provides great advantage such as large surface area, high charge transfer ability and higher chemical stability (Li *et al*. 2014, Lam *et al*. 2016). The heterojunction of carbon based materials and semiconductors can expertly inhibit the recombination rate of charge carriers, which leads to enhancement in catalytic activity of BFO. Shen *et al*. (2013) have synthesized BFO/ graphene nanohybrid via hydrothermal route varying the graphene content, which uplifts the photocatalytic efficiency of pristine BFO towards eradication of congo red. Wang *et al*. (2016) utilized multi walled carbon nanotubes (MWCNTs) and facilitated their utilization to augment the photocatalytic ability of pristine BFO. Dai *et al*. also used graphene to significantly increase photocatalytic efficiency of BFO for mortification of methyl orange, where graphene and CNT played as title character in transportation of electrons to the surface of BFO and thereby increasing the electron-hole pair lifetime as well as the photocatalytic activity of pristine BFO (without CNT/graphene attached) (Dai *et al*. 2013). These engaging results motivated us to explore the characteristics of other carbon based materials.

Furthermore, commercially available carbon based nanomaterials are highly expensive and toxic in nature (Muller *et al*. 2005). In accordance, with the growing

*Corresponding author, Ph.D.,
E-mail: sonal1174@gmail.com; sonal@pu.ac.in

ISSN: 2287-237X (Print), 2287-2388 (Online)

demands replacement of these toxic materials with environment friendly materials is obligatory. In this view, coriander seed powder (CDR) was utilized for the first time in order to augment the catalytic activity of BFO. Coriander is a tropical parsley crop and is successfully grown under a wide range of conditions CSIR 2001.

In the present work, single phase, versatile and highly crystalline BFO, BFO/CNT and BFO/CDR nanoparticles were synthesized via wet chemical method using tartaric acid as reducing agent. Novelty of this work is successful fabrication of eco-friendly BFO/CDR nanocomposites as a versatile catalyst for removal of wide variety of pollutants. Oxidative degradation of dyes, drugs, adsorption of a pesticide and reduction studies of para-nitrophenol were examined. Moreover, recyclability and reusability experiments for all the synthesized nanomaterials were also performed. The comparative catalytic and adsorptive efficiency of synthesized green heterojunction with the nanocomposite of bismuth ferrite and carbon nanotubes were examined thoroughly.

2. Experimental section

2.1 Materials and methods

2.1.1 Reagents used

Bismuth (III) nitrate pentahydrate $Bi(NO_3)_3.5H_2O$ (MERCK), iron(III) nitrate nonahydrate $Fe(NO_3)_3.9H_2O$ (CDH), L(+) tartaric acid (Avra synthesis), multi-walled carbon nanotubes (L = 3.8 μM , real density= 1-2 g cm^{-3}) (HPLC), nitric acid (HNO_3) (VETEC), Sodium Borohydride ($NaBH_4$) (CDH Fine Chemical) Coriander seed powder was purchased from local market, 0.044 mm fine series test sieve (U-Tech), Carbol Fuchsin (Avra synthesis), Reactive black 5 (RB5) (Dye star), Doxorubicin (DR) (Adrim), Ciprofloxacin (CP) (CDH) and Malathion (MTN) purchased from local market of Chandigarh.

2.1.2 Synthesis of BFO and its composites

Preparation of CDR: Coriandrum sativum seeds were washed twice with double distilled water and dried at 40-50 ºC. A fine powder was prepared by grinding the seeds and sieving the obtained powder through fine test sieve (sieve size 0.044 mm).

Synthesis of nanocomposites: Equimolar amounts of $Bi(NO_3)_3.5H_2O$ and $Fe(NO_3)_3.9HO$ were dissolved in minimum amount of water containing nitric acid and L(+)Tartaric acid (in 1:2 molar ratio) varying amounts of CNT or CDR (5, 10, 15 and 20 wt%) were dispersed in the solution using ultrasonicator to obtain a homogeneous dispersion. The obtained solution was then heated on a hot plate with constant magnetic stirring to form a dry powder. The powder was then calcined in a furnace at 500 ºC for 1 h under air atmosphere. Subsequently, the calcined powder was washed with acetic acid followed by water for the removal of impurities and further dried at 80 ºC for 2 - 3 h in a hot air oven (Ortiz-Quiñonez *et al*. 2013).

For comparison purpose, pure bismuth ferrite nano-particles were also synthesized via same method excluding the addition of CNT/CDR and sonication step.

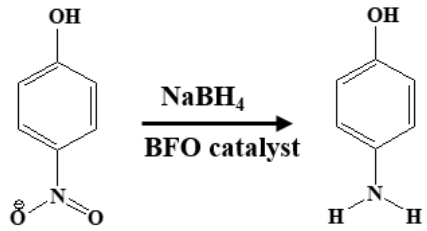

Scheme 1 Reduction reaction of PNP

In order to check the stability, CDR powder was also treated with L+ tartaric acid and nitric acid followed up by the calcination step (at 500 ºC for 1 h). Similar treatment was given to CNT powder.

2.2 Physical measurements

The synthesized nanomaterials were characterized using different techniques to confirm their successful fabrication. The characterization techniques utilized in this work have already been reported in our previous article (Kaur *et al*. 2019). The magnetic studies were conducted by Vibrating Sample Magnetometer (Microsense EZ7). X-ray photoelectron spectroscopy (Thermofisher scientific, Model: Nexsa base) used for XPS studies.

2.3 Experimental methods

The photocatalytic and adsorptive performance of synthesized nanomaterials were examined for various pollutants and the procedures are same as mentioned in our previously published work (Kaur *et al*. 2019). For the reduction of PNP (Scheme. 1), catalytic reduction method using $NaBH_4$ as co-catalyst was followed. In brief, 20 mL PNP solution (0.036 mol L^{-1}) was taken in 100 mL beaker, followed by addition of 1.36 g (50 equivalents) of $NaBH_4$. Subsequently, fixed amount of catalyst was added to the solution. The colour of the solution progressively vanished with time, indicating the reduction of nitro phenol. To examine the progress of reaction, 0.3 μL sample aliquots at fixed time intervals, were withdrawn and analysed via UV–visible spectra (Goyal *et al*. 2014).

3. Results and discussion

3.1 Possible mechanism for formation of BFO/CNT and BFO/CDR

During synthesis of nanocomposites, L+tartric acid was utilized as a chelating agent having two carboxylate and two hydroxyl groups. These carboxylate groups help in formation of homogeneous polyester precursor and their accommodation in favourable condition facilitates the formation of hetrometallic polynecular complex. In the aqueous solution, tartaric acid coordinates with metal nitrates to form bismuth tartrate. Carboxylate group (having four membered ring) and three alkoxide-carboxylate groups (having five membered rings) bidentately coordinate with bismuth (as shown in Fig. 1), which makes the reacting

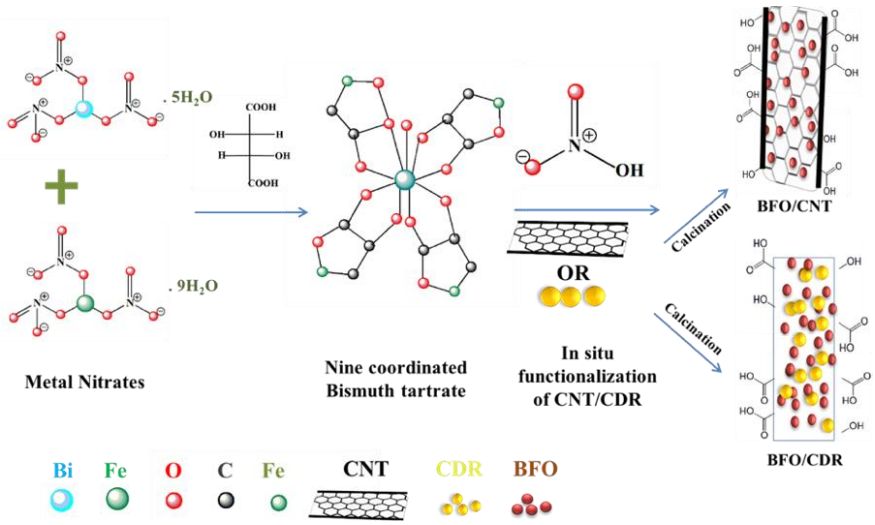

Fig. 1 Possible mechanism for formation of BFO/CNT and BFO/CDR nanocomposite

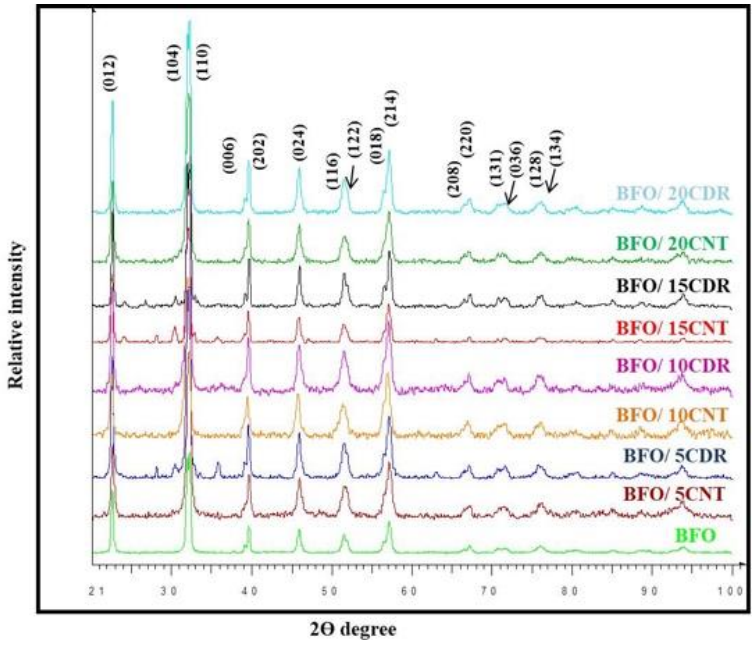

Fig. 2 Powder X-ray patterns of BFO and its nanocomposites

metals available in nearby propinquity. This Bi-Fe-polynuclear complex formed in aqueous solution, dissociates in presence of heat and HNO_3 to form bismuth ferrite (Ghosh *et al*. 2005, Hu *et al*. 2011). Furthermore, in situ covalent functionalization of CNTs and CDR occurred due to presence of nitric acid in reaction mixture, resulted in formation of chemically stable carboxyl and hydroxyl group over the surface of CNT and CDR (Norizan *et al*. 2020). These functionalized CNTs bonded chemically (via covalent bond) with bismuth ferrite and formation of nano-composite takes place (Wang *et al*. 2016). The presence of carboxyl and hydroxyl groups in BFO/CNT and BFO/CDR nanocomposites was also observed by FT-IR spectra Fig. 3(a). Heat treatment (calcination at 500 ºC) leads to evaporation of crystalline water, decomposition of chelate complex and nitrates. Calcination played an important role to grow well crystalized pure BFO (Hu *et al*. 2011).

3.2 Characterizations

3.2.1 Fourier Transform Infrared (FT-IR)

In order to authenticate the presence of functional groups FT-IR technique was employed. The FT-IR spectra of all the synthesized materials are illustrated in Fig. 3(a). Two bands were observed, the higher frequency band ~555.8 cm^{-1} and the lower frequency band ~452.9 cm^{-1} which can be assigned to tetrahedral M–O stretching vibration and octahedral M–O stretching vibration, respectively. It elucidate that the normal mode of vibration of tetrahedral cluster is higher as that of octahedral cluster, which indicates the shorter bond length of tetrahedral cluster as compared to bond length of octahedral cluster (Pradeep *et al*. 2006). The band around 3398 cm^{-1} indicated the presence of hydroxyl groups, whereas band at ~1630 cm^{-1} and 1200 cm^{-1} represent C=O and C-O stretching

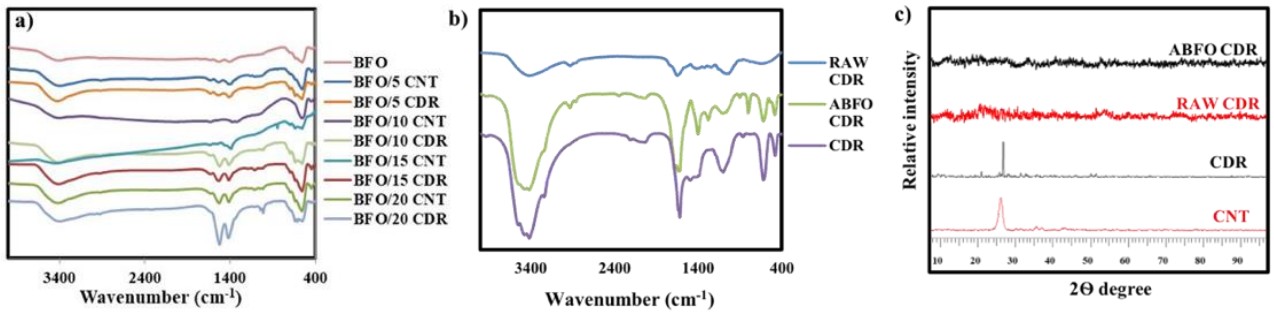

Fig. 3 FT-IR spectra (a) BFO and its nanocomposites, (b) treated CDR (CDR), amorphous BFO 10CDR (ABFO CDR) and raw CDR; (c) XRD pattern of treated CNT, CDR, raw CDR and ABFO 10CDR

vibrations, presence of L+ tartaric acid and in situ oxidation of CNTs and CDR due to presence of HNO_3 could be the possible reason for these bands (Avilés *et al*. 2009) (Kang *et al*. 2015).Increase in intensity of the above mentioned IR band was observed with increase in the amount of CNT/CDR, which correlates with the increase in number of C=O and C-O bonds. Furthermore, in order to get a better insight, FT-IR spectra of raw CDR (RAW CDR), amorphous BFO 10CDR (abbreviated as ABFO CDR) and treated CDR (CDR) were also analysed and presented in Fig. 3 (b). FT-IR bands obtained in case of RAW CDR were of very low intensity, while, in case of ABFO CDR much intense bands were obtained, suggesting the oxidation of CDR in presence of nitric acid. The intense band ~1395 cm^{-1} could be assign to C-H symmetric bending (Hu *et al*. 2011). While, disappearance of bands at 1277 and 2926 cm^{-1}, in case of treated CDR, indicates the removal or breakage of some C=O and C-H due to annealing. Removal of these oxygen functionalities due to heat treatment, may generate new active sites beneficial for catalysis.

3.2.2 Powder X-ray diffraction (PXRD)

The room temperature XRD pattern of all the synthesized BFO nanoparticles and its composites are depicted in Fig. 2. The observed patterns were in good harmony with that of pure phase of BFO (JCPDS No. 01-071-2494). The obtained pattern confirmed the development of single phase BFO with high crystallinity. No additional peaks were observed, thus ruling out the presence of any secondary phase indicating a pure rhombohedral perovskite structure of the synthesized materials having space group R3c. It was observed from PXRD patterns that the presence of CNT and CDR does not affect the phase structure of BFO (Wang *et al*. 2016, Guo *et al*. 2020). Further the lattice parameters of pure BFO were calculated using the inbuilt software TOPAS 2.1 (a = b = 5.58567 G ± 0.00002 Å and c = 13.88767 Å G± 0.00005 Å). The crystallite size of all the synthesized nanomaterials was calculated by considering the most prominent peak at 32° indexed to 110 plane using the well-known Debye Scherrer's equation (Strømme *et al*. 1995) (Kaur *et al*. 2019) and it was found to be in the range of 13.3 - 13.6 nm. To enquire the stability and phase formation of carbonaceous materials under reaction condition, XRD pattern of treated CNTs and CDR powder were also observed and showcased in Fig. 3(C). The most prominent peak ~26.3° indicates the graphite form of carbon as reported in the literature (Soliemani *et al*. 2015).

The observed XRD patterns of CNT and CDR were found to be in good harmony with each other indicating the formation of similar phase of carbon. Furthermore, to investigate the role of calcination, XRD patterns of raw CDR and ABFO CDR were also examined. Broad continuum were observed in both the cases confirmed their amorphous nature (Fig. 3(c)), similar results were obtained by Hu *et al*. (2011) for BFO. While after heat treatment of ABFO CDR (at 500 °C), highly crystalline BFO 10CDR was formed, as shown in Fig. 2.

3.2.3 Field Emission Scanning Electron Microscopic (FESEM)

Field emission scanning electron microscopy technique was employed for investigation of the morphological aspect of synthesized bare BFO and its composites with CNT and CDR. The obtained scanning electron micrographs of synthesized materials are depicted in Fig. 4. The uniform growth of BFO nanoparticles can be observed, having random shape with edges and particles were observed to be in agglomerated form due to inherent magnetism, Fig. 4(b) shows homogeneous growth of BFO particles in matrix of MWCNT whereas Fig. 4(c) displays homogenous growth of BFO particles in CDR matrix. Furthermore, to analyze the surface morphology of CDR powder FE-SEM micrographs of treated CDR at different resolution were also depicted in Fig. 5(a) and (b). Particles were found to be of random shape. The EDX spectra of the synthesized materials are depicted in Fig. 4(f) and (i). The presence of carbon content in case of both the nanocomposites was observed from the EDX spectra and no additional peaks corresponding to other elements was seen, thus ruling out the presence of impurities. Elemental mapping of synthesized nano-composites indicates symmetric distribution of carbon content into the matrix as presented in Fig. 4(d)-(h).

3.2.4 Vibrating Sample Magnetometer (VSM)

Vibrating Sample Magnetometer was used to examine magnetic properties of synthesized BFO and its composites. The hysteresis curves at room temperature are depicted in Fig. 5(e). The saturation magnetization value was found to be highest in case of pure BFO i.e., 1.73 emu/g. Table 1 showed a gentle decay in the m_s value with addition of CNT/CDR, attributable to the non-magnetic character of

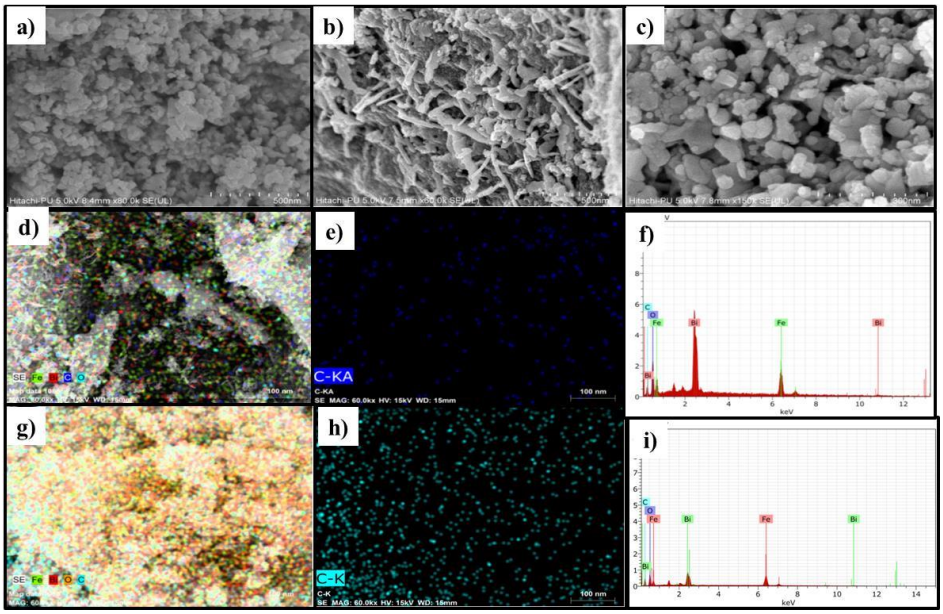

Fig. 4 FE-SEM micrographs of (a, b, c) pure BFO, BFO/10 CNT, BFO/10 CDR and mapping images of (d, e) BFO/10 CNT and (g, h) BFO/10 CDR); (f, i) EDX spectra of BFO/10 CNT and BFO/10 CDR.

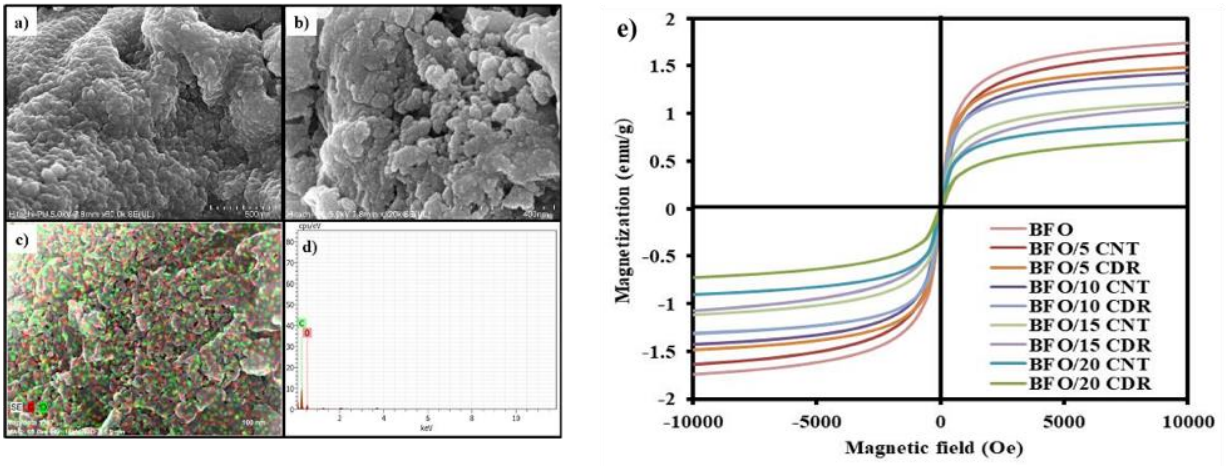

Fig. 5 FE-SEM micrographs of CDR at (a) 500 nm, (b) 400 nm, (c) mapping and (d) elemental analysis, (e) hysteresis loops for BFO and its nanocomposites

both CNT and CDR still the samples are sufficiently magnetic to be recovered using external magnet and reused. The observed decay in value of saturation magnetization also confirmed the successful fabrication of BFO nano-composites. The magnetic interparticle interaction was examined through the squareness ratio, which represents different types of intergrain group exchanges. The values of squareness ratio were observed to be less than 0.5 for all the synthesized nanomaterials, which is indicative of magnetostatic interaction between the particles, small single- domain, and randomly oriented assembly of spherical particles (Tenorio-González *et al*. 2017).

3.2.5 CHNS/O Elemental Analysis (CHNS)

In order to examine chemical composition of RAW CDR and treated CDR, CHNS analysis was caried out and obtained results are presented in Fig. 6(d) The decrease in carbon % in case of treated CDR may be due to reduction during calcination, while increase in nitrogen and oxygen % could be attributed to oxidation of CDR in presence of nitric acid. Results are in good agreement with FTIR studies, showcased more intense bands corresponding to oxygen functionalities in case of treated CDR.

3.2.6 Diffuse Reflectance Spectroscopy (DRS)

The light absorption properties of prepared BFO and its nanocomposites were investigated at room temperature using UV-visible Diffuse Reflectance Spectra (DRS). Tauc equation (Eq. (1)) was utilized to determine the band gap energy of synthesized materials (Harish *et al*. 2012) (Tauc *et al*. 1966).

$$(\alpha)h\upsilon = A(h\upsilon - E_g)^{1/2} \quad (1)$$

$(\alpha h\upsilon)^2$ *vs*. photon energy $h\upsilon$ plots were utilized for the evaluation of the band gap as presented in Figs. 6(a)-(c).

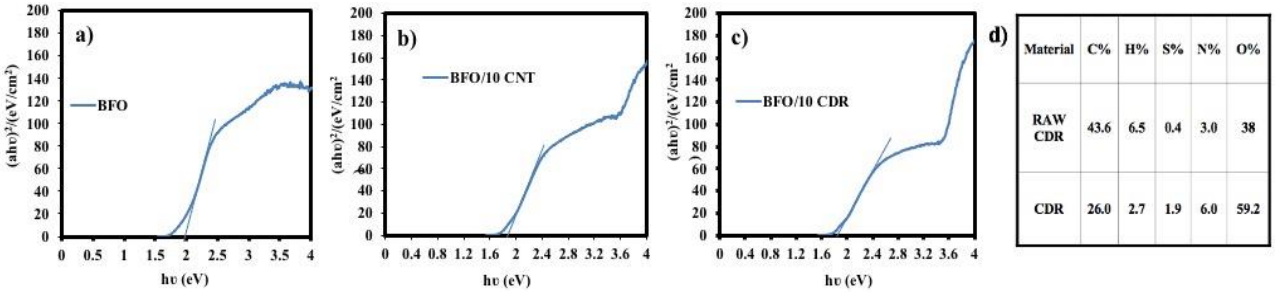

d)

Material	C%	H%	S%	N%	O%
RAW CDR	43.6	6.5	0.4	3.0	38
CDR	26.0	2.7	1.9	6.0	59.2

Fig. 6 Diffuse reflectance pattern of (a) BFO nanoparticles (b) BFO/10 CNT and (c) BFO/10 CDR respectively, (d) CHSN/O data of RAW CDR and treated CDR (CDR)

Table 1 Saturation magnetization ($m_{s)}$, remanence (m_r), coercivity (h_c), squareness ratio (S) and band gap (eV) values for synthesized BFO and its nanocomposites

Catalyst	m_s (emu/g)	m_r (emu/g)	h_c (oe)	S = $(m_r/m_s)*10^{-2}$	Band gap (eV)
BFO	1.73	0.024	20	0.013	2.05
BFO/5 CNT	1.63	0.270	29	0.160	1.96
BFO/5 CDR	1.48	0.049	40	0.033	1.92
BFO/10 CNT	1.47	0.078	50	0.053	1.82
BFO/10 CDR	1.11	0.009	27	0.008	1.83
BFO/15 CNT	1.46	0.135	78	0.092	1.95
BFO/15 CDR	0.90	0.044	45	0.048	1.97
BFO/20 CNT	1.30	0.113	75	0.088	2.19
BFO/20 CDR	0.71	0.029	61	0.040	2.10

By analyzing the obtained plots their corresponding band gap values E_g (eV) were recorded and listed in Table 1. The band gap value for BFO was obtained to be 2.05 eV, which was consistent with the reports (Irfan *et al*. 2019).

A much smaller band gap values 1.82 eV and 1.83 eV were obtained for the 10 wt% BFO/CNT and 10 wt% BFO/CDR, respectively. The proficient decay in the band gap energies of modified BFO was due to induction of external energy levels with addition of carbon based materials, which contributes towards enhanced photo-catalytic performance of synthesized nanocomposites. BFO attached with carbonaceous materials results in formation of Fe–O–C bonds at the surface of the BFO nanoparticles. As C–O contains strong covalent bonds, charge transfer from the oxygen ligand to the Fe ions may be further reduced in BFO, which results in the decrease in band gap (Wang *et al*. 2016). Analogous results were observed in case of the BFO/CNT and BFO/CDR composites. Previously reported studies suggests that addition of graphene with BFO leads to chemical bonding between BFO and specific sites of carbon which results in significant decrease in the band gap value of BFO (Li *et al*. 2013, Wang *et al*. 2016). The addition of CDR and CNT significantly altered the band gap of synthesized nanoparticles and thus possessing the potential to act as better visible light driven photocatalyst compared to pristine BFO.

3.2.7 Cyclic Voltammetric (CV)

The charge transfer characteristics and surface area of the synthesized nanoparticles were determined by utilizing traditional three electrode system. Pt wire was employed as counter electrode and Ag/AgCl/KCl as reference electrode. The glassy carbon electrode (GCE) was modified separately with dispersion of BFO and BFO nanocomposites (10 mg mL^{-1}) in water within potential range from 1.2 mV to -1.2 mV at a scan rate of 10 mV s^{-1} in redox solution (0.1 M KCl in 5.0 mM $[Fe(CN)_6]^{3-}$). The CV curves shown in Fig. 7(a) exhibits an increase in faradic response for BFO modified with CNT and CDR nanocomposites, suggesting remarkable boost in electron transportation rate and increase in the electron transfer characteristics. The CV studies were further employed for the computation of surface area of the synthesized nanoparticles by covering the range of the scan rate from 10 to 100 mV s^{-1} presented in Fig. 7(b).The surface area of modified GCE with BFO and nanocomposites was calculated using slope values of the peak current (Ip) vs. square root of scan rate ($v^{1/2}$) in Randle-Sevcik equation (Eq. (2)) (Randles 1948) (Ševčík 1948) (Delahay *et al*.1951).

$$I_p = 2.69 \times 10^5 AD^{1/2}n^{3/2}v^{1/2}C \quad (2)$$

where, I_p represents the current response (ampere), D denotes the diffusion coefficient (cm^2 s^{-1}) of supporting electrolyte solution, C is the supporting electrolyte concentration (mol cm^{-3}), n is the count of electrons participated in the redox phenomenon, A and v represent the area of electrode (cm^2) and scan rate (V s^{-1}), respectively (Prakash *et al*. 2018).

The surface area of BFO/GCE was found to be 0.00811 cm^2 whereas incredible enhancement in the surface was

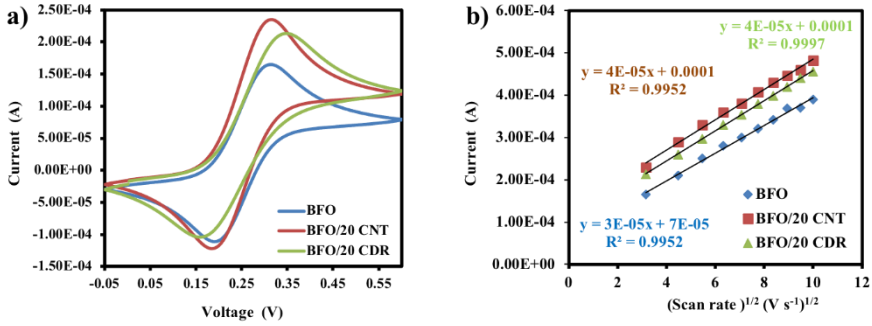

Fig. 7 Cyclic voltammetric curves for different modified electrodes in (a) (0.1 M KCl in 5.0 mM $[Fe(CN)_6]^{3-}$) at scan rate of 10 mV s^{-1} and (b) plot of anodic (Ip_a) peak current *vs.* square root of scan rate (V s^{-1})$^{1/2}$

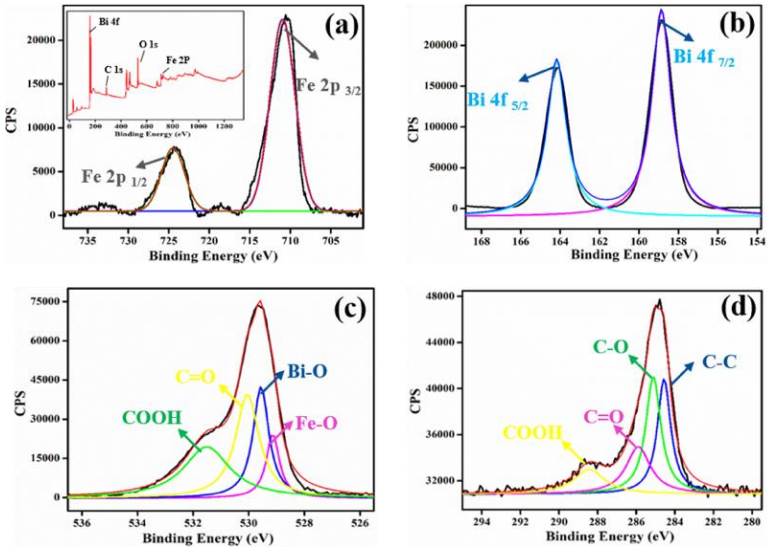

Fig. 8 Deconvoluted XPS spectra of BFO/10CDR (a) Fe 2p (inset showing the survey scan of BFO/10 CDR), (b) Bi 4f, (c) O 1s and (d) C 1s

observed in case of BFO/20 CNT and BFO/20 CDR nanocomposites. An increment in the surface area from 0.008 cm^2 to 0.018 cm^2 was observed for both BFO/CNT and BFO/CDR nanocomposites, which was quite expected as a reason of introduction of high surface area possessed carbonaceous material in the BFO nanoparticles. Equal enhancement in surface area was observed with addition of equal amount of CNT or CDR. Since process of adsorption symmetrically related to the surface area of adsorbent, so it was predictable that the adsorbent with the high surface area value would possess high adsorption characteristics (Komal *et al*. 2020).

3.2.8 X-ray Photoelectron Spectroscopy (XPS)

XPS analysis was utilized to examine the valance state of elements in BFO/CDR nanocomposites. Survey scan revealed the presence of C 1s, Fe 2p, O 1s and Bi 4f (inset of Fig. 8(a). The peaks of Fe 2p spectra corresponding to Fe $2p_{3/2}$ and Fe $2p_{1/2}$ with binding energies at 710.9 and 724.4 eV for BFO/CDR were observed in Fig. 8(a), indicating the presence of Fe^{3+} (Wang *et al* 2016). Whereas, in case of Bi 4f spectrum, Fig. 8(b), peaks corresponding to Bi $4f_{5/2}$ and Bi $4f_{7/2}$ (which usually exhibit at 163.7 and 158.7 eV in pristine BFO) were observed at 164.1 and 158.88 eV, respectively, indicating the presence of Bi^{3+} state, a significant shift towards higher binding energy was observed suggesting certain chemical interaction between BFO and CDR. In the deconvoluted XPS spectrum of O 1s four peaks were observed corresponding to Bi-O, Fe-O, C=O and COOH, depicted in Fig. 8(c). The peak corresponding to Bi-O and Fe-O were observed at 529.1 and 529.5 eV (which usually exhibit at 530.5 and 529.9 eV in case of pristine BFO (Wang *et al* 2016), indicating oxygen-metal bonds of BFO/CDR shifted towards lower binding energy as that of BFO. The electronic interactions between CDR and BFO could be the possible reason behind this significant shift, indicating the formation of Bi-O-C and Fe-O-C bonds, thus, confirming the formation of BFO/CDR heterojunction (Mukherjee *et al*. 2018). The deconvoluted peaks at 530 and 531.5 eV corresponding to C=O and COOH indicating the oxygen containing groups of CDR, Fig. 8(c). The high resolution C 1s spectra, showcased the presence of deconvoluted peaks at 284.5, 285.1, 285.9 and288.4 eV corresponding to C-C, C-O, C=O and COOH, respectively (Wang *et al.* 2016, Han *et al*. 2019, Jackson and Nuzzo 1995). The peak at 284.5 eV is related to graphitic form of carbon (in agreement with XRD shown in Fig. 3(c)), whereas remaining peaks arise due to oxygenated species confirming the in-situ oxidation of CDR.

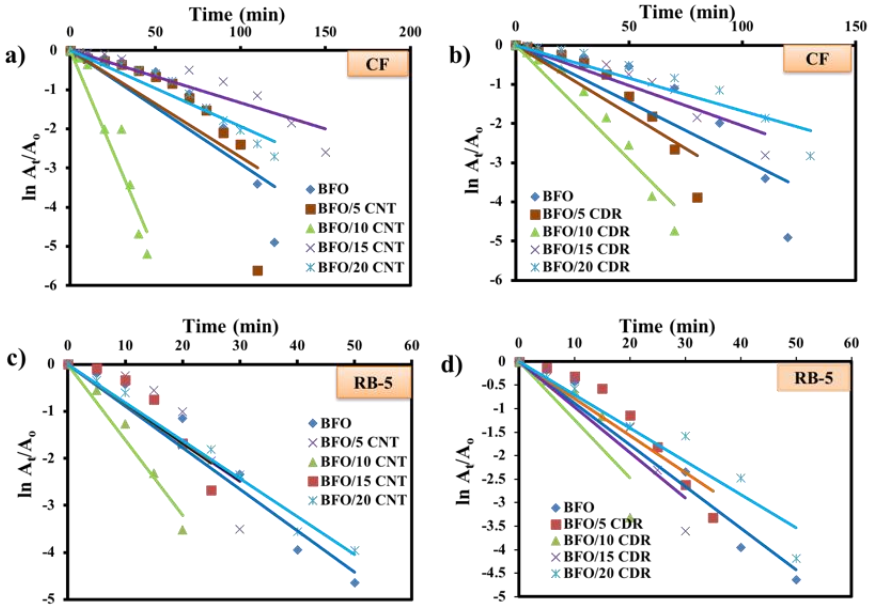

Fig. 9 Pseudo first order kinetic curves for the photocatalytic degradation of CF and RB5 using (a, c) BFO/CNT nanoparticles and (b, d) BFO/CDR nanoparticles

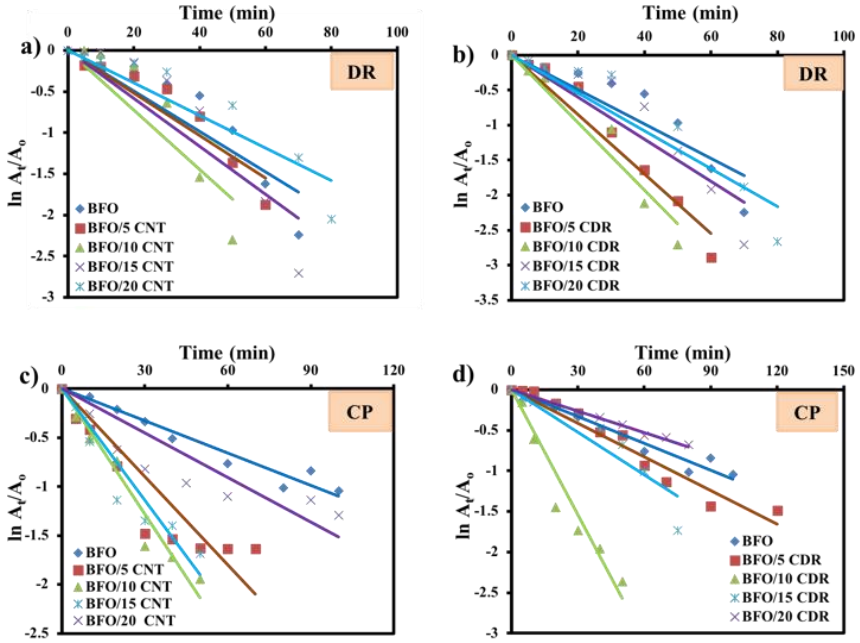

Fig. 10 Pseudo first order kinetic curves for the photocatalytic degradation of DR and CP using (a, c) BFO/CNT nanoparticles and (b, d) BFO/CDR nanoparticles

4. Comparative evaluation of catalytic activity of the synthesized materials: Oxidative degradation studies

The photocatalytic activity of all the synthesized materials was examined for the degradation of dyes Carbol fuchsin (CF 16 mg/L), Reactive black (RB5 60 mg/L), and drugs Ciprofloxacin (CP 10 mg/L), Doxorubicin (DR 50 mg/L), under visible light irradiation. The absorption maxima for CF, RB5, CP and DR were observed at ~550, 597, 278 and 500 nm respectively.

In order to examine comparative catalytic activity of synthesized materials, oxidative degradation of CF, RB5, CP, DR as pollutant sample was performed under visible-light irradiation. BFO/10 CNT and BFO/10 CDR showcased highest rate constant values for all model pollutants. Table 2 displays percentage degradation (%), completion time and their corresponding rate constant values for the removal of CF, RB5, DR, CP using bare BFO and its composites. % degradation was calculated by using the following equation (Eq. (3)).

$$\%\text{Degradation} = \frac{A_0 - A_t}{A_0} * 100 \quad (3)$$

The results demonstrated that 10 wt% addition of CNT

Table 2 Percentage degradation, completion time and their corresponding rate constant values for the degradation of CF, RB5 dyes and DR, CP drug using BFO and its nanocomposites

Catalyst	CF		RB5		DR		CP	
	Rate constant $k*10^{-2}$ (min^{-1}) (R^2)	Completion time (min) (removal %)	Rate constant $k*10^{-2}$ (min^{-1}) (R^2)	Completion time (min) (removal %)	Rate constant $k*10^{-2}$ (min^{-1})(R^2)	Completion time (min) (removal %)	Rate constant $k*10^{-2}$ (min^{-1})(R^2)	Completion time (min) (removal %)
BFO	2.9(0.85)	120(99.2)	8.8(0.95)	50(99.0)	2.4(0.85)	70(89.3)	1.1(0.97)	100(64.7)
BFO/5 CNT	2.7(0.7)	110(99.6)	8.2(0.80)	30(97.0)	2.5(0.89)	60(84.6)	3.0(0.81)	70(80.4)
BFO/5 CDR	3.5(0.85)	80(99.9)	7.8(0.88)	35(96.3)	4.2(0.97)	60(94.4)	1.3(0.96)	120(49.3)
BFO/10 CNT	10.3(0.91)	45(99.4)	16(0.96)	20(97.0)	3.6(0.84)	50(90.0)	4.1(0.97)	50(82.5)
BFO/10 CDR	5.8(0.92)	70(99.1)	12.3(0.8)	20(96.3)	4.8(0.93)	50(93.3)	5.1(0.97)	50(90.5)
BFO/15 CNT	1.3(0.87)	120(93.3)	8.4(0.85)	25(93.1)	2.9(0.85)	70(93.3)	3.8(0.91)	50(81.4)
BFO/15 CDR	2.0(0.90)	110(94.0)	9.6(0.87)	30(97.2)	3.0(0.86)	70(93.3)	1.7(0.89)	75(82.3)
BFO/20 CNT	1.9(0.93)	150(92.6)	8.1(0.98)	50(98.0)	1.9(0.86)	80(87.1)	1.5(0.7)	100(72.6)
BFO/20 CDR	1.6(0.91)	120(94.9)	8.1(0.93)	50(98.4)	2.7(0.9)	80(93.0)	0.8(0.98)	80(77.3)

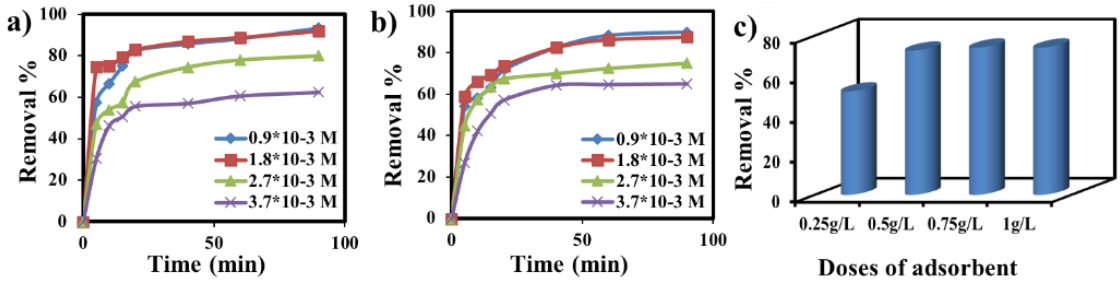

Fig. 11 Effect of adsorbent loading on the adsorption of MTN using BFO (initial concentration=1.8×10^{-3} M and pH = 7) (c) effect of initial pollutant concentration on the percentage adsorption (%) of MTN using (a) BFO/20 CNT and (b) BFO/20 CDR respectively (dosage of adsorbent = 0.5 g/L at pH = 7)

and CDR were most efficient for the eradication of noxious effluents, similar outcomes were found in literature for BFO/CNT (Wang *et al*. 2016), whereas such results using BFO/CDR nanocomposites have never been reported earlier. Further increase in the weight ratio of CNTs and CDR weaken the photocatalytic activity of the nano-composites. The dramatical enhancement in the catalytic activity can be explained on the basis of band gap and CV studies. The band gap values were observed to decrease with the introduction of both CNT and CDR which results in the higher electron transfer kinetics during photo-catalysis. The CV studies showed a significant increase in the current values of redox peaks with the introduction of CNT and CDR which indicates the enhancement in charge transfer rate (Prakash *et al*. 2018).

4.1 Kinetic studies

The photocatalytic degradation of CF, RB5, CP, and DR was found to follow pseudo-first order kinetics. The values of rate constant were calculated by (Eq. (4)) (Noorimotlagh *et al*. 2018, Corbett 1972).

$$ln\frac{A_t}{A_0} = -kT \tag{4}$$

By plotting $\ln(A_t/A_0)$ as a function of time (min) Figs. 9 and 10 the values of rate constant k (min^{-1}) were obtained from the slopes of the lines are mentioned in the Table 2. The rate constant values shows incredible enhancement in the catalytic efficiency of pristine BFO with the addition of 10 wt% CNT and CDR as mentioned in Table 2. Maximum value of rate constant were observed as $10.3*10^{-2}$, $16.0*10^{-2}$, $4.8*10^{-2}$, $5.1*10^{-2}$ min^{-1} for, CF, RB5, DR and CP respectively.

4.1.1 Total organic carbon analysis

In order to investigate the amount of carbon degraded during photocatalytic degradation reaction TOC analysis was performed utilizing combustion catalytic oxidation method (through Simadzu TOC-L analyzer) and % removal of TOC was calculated using Eq. (5). The results obtained for RB-5 dye utilizing BFO and BFO 10CDR (after 20 min and 60 min of photocatalytic degradation) are depicted in Fig. 16(c). 62.1% removal of organic carbon in 60 min was

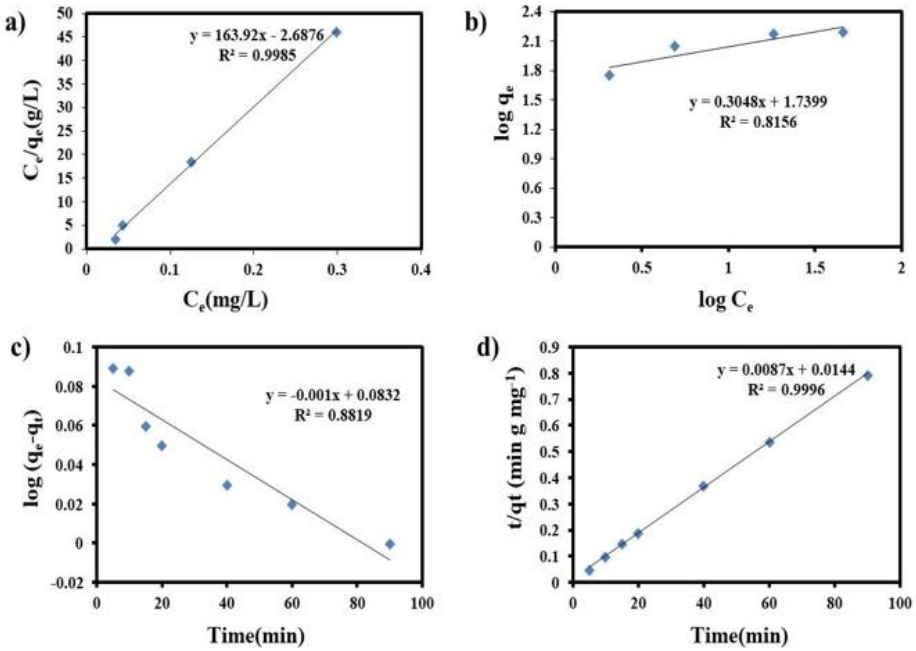

Fig. 12 (a, b) Langmuir and Freundlich adsorption isotherms; (c, d) pseudo-first-order kinetics and pseudo second order for the adsorption of MTN, using BFO/20 CNT (dosage of adsorbent = 0.5 g L^{-1} at pH = 7, initial concentration = 1.8×10^{-3} M)

Table 3 Different adsorption parameters obtained from Langmuir and Freundlich isotherms for adsorption of MTN on surface of BFO/20 CNT and BFO/20 CDR

Adsorbent	K_L (Lmg^{-1})	q_m (mg g^{-1})	R_L	R^2	K_F (mg g^{-1}) (L $mg^{-1})^{1/n}$	n	R^2
BFO/20CNT	2.6	163.92	$6.21*10^{-3}$	0.998	1.73	0.304	0.8156
BFO/20CDR	8.955	192.6	$1.96*10^{-3}$	0.987	1.524	0.437	0.864

Table 4 Different adsorption parameters obtained from pseudo first order and pseudo second order kinetic model for adsorption of malathion on surface of BFO/20 CNT and BFO/20 CDR.

Adsorbent	q_e (mg g^{-1})	K_1 (min^{-1})	R^2	q_e (mg g^{-1})	K_2 (g mg^{-1}) (min^{-1})	R^2
BFO/20 CNT	0.0144	0.0087	0.881	0.0832	0.001	0.999
BFO/20 CDR	0.139	0.0019	0.7926	0.0378	0.0096	0.999

Table 5 Percentage reduction, completion time and their corresponding rate constant for reduction of PNP; adsorption % of malathion using synthesized nanoparticles

Catalyst	Removal percentage of PNP (Time min)	Rate constant ($k*10^{-2}$) (min^{-1})	Adsorption % of MTN (in 90 min)	R^2
BFO	89.0 (60)	3.8	72.5	0.82
(BFO/5 CNT	91.5 (5)	51.3	73.5	0.87
BFO/5 CDR	90.5 (12)	23.1	75.0	0.89
BFO/10 CNT	99.9 (5)	47.4	78.3	0.98
BFO/10 CDR	99.9 (5)	39.8	77.0	0.96
BFO/15 CNT	91.0 (12)	21.4	86.2	0.95
BFO/15 CDR	91.4 (9)	32.5	77.9	0.75
BFO/20 CNT	85.7 (10)	22.6	91.5	0.85
BFO/20 CDR	82.8 (10)	19.7	87.5	0.92

observed for BFO, while a much higher value of 79.7% was observed for BFO 10CDR, the obtained results clearly suggest that BFO 10CDR showcased higher degradation of organic carbon as that of pristine BFO.

$$\%Removal\ of\ Carbon \tag{5}$$

$$= [\frac{TOC\ in\ water\ before\ treatment - TOC\ in\ water\ after\ treatment}{TOC\ before\ treatment} * 100]$$

4.2 Mechanism for oxidative degradation

Besides having efficient utilization in light harvesting and adsorption capacities, the presiding contribution of carbon based materials in BFO/CNT and BFO/CDR nanocomposites towards oxidative degradation is separating the ions. In presence of light, electrons (e^-) get energized and jumped from the valence band to conduction band, creating a vacancy (h^+) in the valence band. Li *et al*. (2014) reported that these photoexcited electron and holes have strong tendency to recombine, leading to the unavailability of charge carriers during photodegradation, and hence offer decent reactivity. However in case of BFO/ CNT and BFO/CDR nanocomposites, when the light falls on the reaction mixture it generates electrons and these electrons may get transferred to the CNT and CDR. Furthermore these transferred electrons (e^-) combines with the confined oxygen within the nanocomposite, and form anionic superoxide radical ($O_2^{\cdot-}$), and thus decelerate the recombination process of electron and holes (Dai *et al*. 2013). Further, H^+ combines with $O_2^{\cdot-}$ and formation of $HO_2^{\cdot}$ take place and subsequent protonation leads to formation of the hydrogen peroxide. Which increase the production of hydroxyl radicals ($^{\cdot}OH$) that promptly oxidizes the pollutant molecules as reported in literature (Wang *et al*. 2016).

4.3 Photocatalytic degradation of pollutant mixture

In order to evaluate the practical application of synthesized nanoparticles, mixture of textile (RB5+CF; 50 mL solution each) and mixture of pharmaceutical waste (DR+CP; 50 mL solution each) was treated by utilizing BFO/10 CDR. Furthermore, the degradation profile for mixture of dyes and drugs (RB5+CF+ DR+CP; 25 mL solution each) was also evaluated and illustrated in Fig. 10. Fig. 16(a) showcased the degradation profile of mixture of dyes and mixture of drugs, respectively. The fabricated nanocatalyst was found to be highly efficient even for degradation of mixture of textile and pharmaceutical waste. Percentage removal and degradation time for mixture was calculated and is presented in Table 6.

5. Adsorption studies

Extensive usage of pesticides and weedicides for agricultural purpose is highly responsible for contaminated ground water. Owing to toxic nature and their entry into the food chain pesticide contamination has reached to a scary stage (Huang *et al*. 2018). The concentration of pesticides in portable water should be lower than 0.1µg/L according to EEC directive (Chatterjee *et al*. 2010). However, due to complex structure of the pesticides single method is not enough for the removal purpose. Adsorption is an efficient way for removal of organic contamination from water due to its low cost and easy implementation. In the present study BFO nanoparticles and its nanocomposites with CNT and CDR were employed for the very first time for the adsorption of a widely used pesticide Malathion (MTN).

The typical UV–visible absorption maximum of MTN was observed at ~190 nm. A gradual decrease in the absorbance values was observed indicating the removal of MTN. The adsorption was carried out at varying concentrations of MTN, on the surface of BFO/20 CNT and BFO/20 CDR (at neutral pH). The amount of adsorption (%Ads) was computed using the under given relation (Eq. (6)).

$$\%Ads = \frac{A_0 - A_t}{A_t} * 100 \quad (6)$$

where A_0 and A_t represent the initial absorbance of MTN solution and absorbance of MTN solution at time t (mg/L), respectively. The highest percentage adsorption of MTN was observed to be around 91.9% and 88.46% by using BFO/20 CNT and BFO/20 CDR as adsorbents, respectively. The adsorption capacity can be harmonized to the quantity of adsorbate (MTN) taken up by the adsorbent. Mass balance equations given below (Eqs. (7) and (8)) were employed to calculate the catalyst adsorption capacities (q_t) at specific time and at equilibrium (q_e) (Niaei and Rostamizadeh 2020).

$$q_t = \frac{(C_0 - C_t)}{m} * V \quad (7)$$

$$q_e = \frac{(C_0 - C_e)}{m} * V \quad (8)$$

where C_0 and C_t represent the initial and concentration of MTN solution and concentration of MTN solution at time t, m and V represent the mass (dried pollutant in g) and volume of pollutant solution taken for experiments (L), respectively.

5.1 Adsorption parameters

All the adsorption studies were conducted at neutral pH and room temperature (300 K). The outcomes were analyzed by varying the amount of adsorbent, adsorbate and contact time (Fig. 10).

Effect of adsorbent dosage:

As the process of adsorption is surface dependent, the amount of adsorbent is an essential parameter while studying adsorption phenomenon. Keeping the initial concentration of MTN fixed (1.8×10^{-3} M) as Fig. 11 (c) depicts. Initially, the removal percentage of MTN was observed to increase abruptly (52% to 74%), with increase in the amount of adsorbent (0.25 g L^{-1} to 0.5 g L^{-1}). Which was quite obvious as with increased amount of adsorbent availability of active sites get increased and hence the adsorption rate. However, with further increase in the adsorbent quantity from 0.5 g L^{-1} to 1.0 g L^{-1}, nominal enhancement in the adsorption percentage was observed may be due to unavailability of adsorbate molecules owing to the aggregation of adsorbent particles, or may be due to overloading of surface binding sites (Padmavathy *et al*. 2016). Hence, 0.5 g L^{-1} of BFO/20 CNT and BFO/20 CDR was used for further experiments.

Effect of pollutant concentration:

The effect of MTN concentration on the adsorption

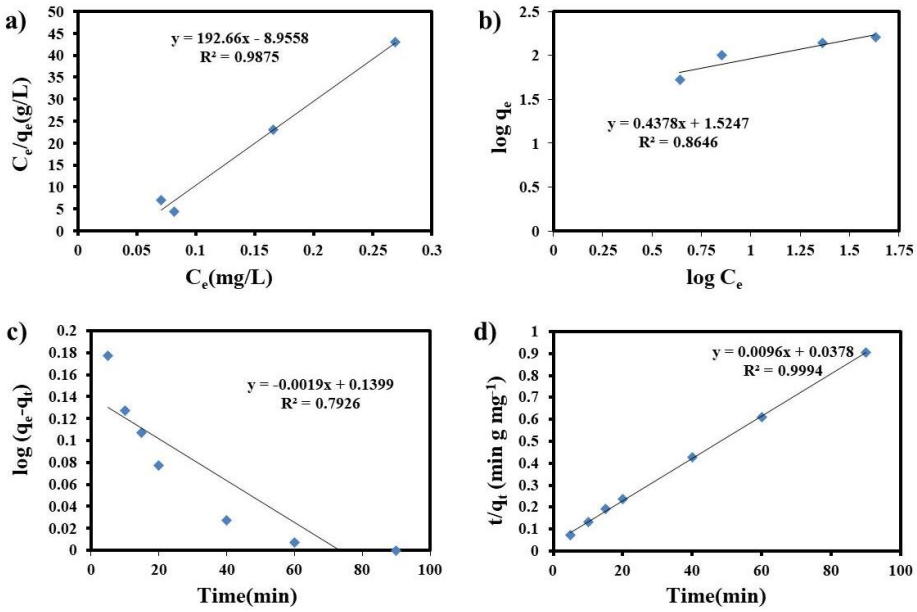

Fig. 13 (a, b) Langmuir and Freundlich adsorption isotherms; (c, d) pseudo-first-order kinetics and pseudo second order for the adsorption of MTN, using BFO/20 CDR (dosage of adsorbent = 0.5 g L^{-1} at pH = 7, initial concentration = 1.8×10^{-3}

phenomena was examined to look over/into the adsorption isotherms. Experiments were conducted by increasing the concentration of MTN from 0.9×10^{-3} M to 3.7×10^{-3} M using BFO/20 CNT and BFO/20 CDR (adsorbent dosage = 0.5 g L^{-1}, pH = 7) as adsorbent, as displayed in Fig. 11(a), Fig. 11(b). The results demonstrated that the percentage adsorption was maximum for lowest concentration (0.9×10^{-3} M) of MTN, which could be the result of excessively available adsorbent sites at lower concentration of MTN. Moreover, decrease in removal percentage was observed with increase in pollutant concentration which is in support with earlier reports. This may be the result of saturation in active sites, as the amount of adsorbent was fixed for increasing concentration of adsorbate (Komal *et al*. 2020). Hence adsorption percentage decreases with increase in MTN concentration.

Effect of contact time:

Adsorption tendency of an adsorbent highly depends on the contact time between adsorbent and adsorbate. The contact time between adsorbent and adsorbate significantly affect the adsorption capacity of an adsorbent. The impact of contact time for adsorption of MTN on the surface of BFO/20 CNT and BFO/20 CDR (Adsorbent amount = 50mg, pH = 7, pollutant concentration = 8×10^{-3} M) is shown in Figs. 11(a) and (b). The adsorption of MTN was observed 91.25 and 88.46% within 90 min for BFO/20 CNT and BFO/20 CDR, respectively. From Figs. 11(a) and (b) it can be clearly observed that adsorption rate of MTN was significantly high during the initial stage, then gradually slowdown and attains equilibrium. The declination in adsorption rate with time was due to the saturation in active adsorbent sites, which were abundant at initial stage of process. This abrupt adsorption in initial few minutes denotes the chemical nature of adsorption (Komal *et al*. 2020).

Effect of carbon concentration:

The effect of CNT and CDR concentration present in the nanocomposite on the percentage adsorption was observed by testifying the adsorption capacity of all the nano-composites towards adsorption of MTN. Table 5 shows that all the adsorbents were highly efficient for the adsorption of MTN at neutral pH. 72.5% adsorption of MTN was observed for the pristine BFO nanoparticles, whereas the highest adsorption efficiency 91.92% and 88.46% was observed for BFO/20 CNT and BFO/20 CDR, respectively. The viable reason for this augmented adsorption could be the increased surface area of the nanocomposites with introduction of carbonaceous materials. The CV results also revealed the proficient augmentation in the surface area of pristine BFO with addition of CNT and CDR. It is quite obvious that with the increased amount of CNT and CDR, surface area increases which leads to hike in superficial active sites of the adsorbent which results in higher adsorption capacities. Thus, amongst all the synthesized nanocomposites, BFO/20 CNT and BFO/20 CDR possessed highest adsorption efficiency.

The obtained results demonstrated that 0.5 g L^{-1} adsorbent loading provided best results (Fig. 11), while the highest adsorption efficiency was observed for BFO/20 CNT and BFO/20 CDR, respectively. Detailed description of these optimization studies are discussed in EPM. Furthermore, the adsorption isotherms and kinetic models were adopted in order to construct the mechanism of adsorption.

5.2 Adsorption isotherm modelling

Two well-known adsorption isotherm models were adopted i.e., Langmuir (Eq. (9)) and Freundlich (Eq. (10)) to structure the detailed description of adsorption phenomenon.

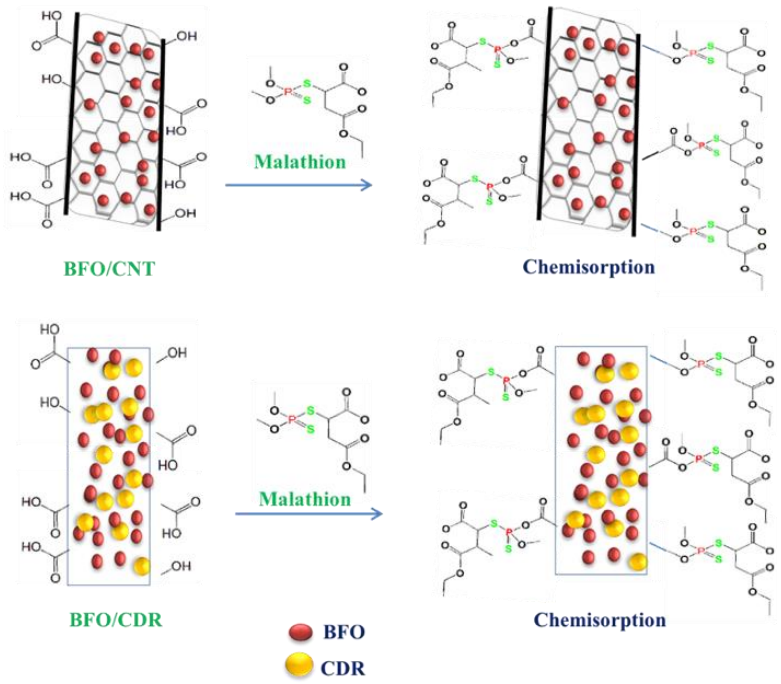

Fig. 14 Plausible mechanism for adsorption of malathion on BFO/CNT and BFO/CDR

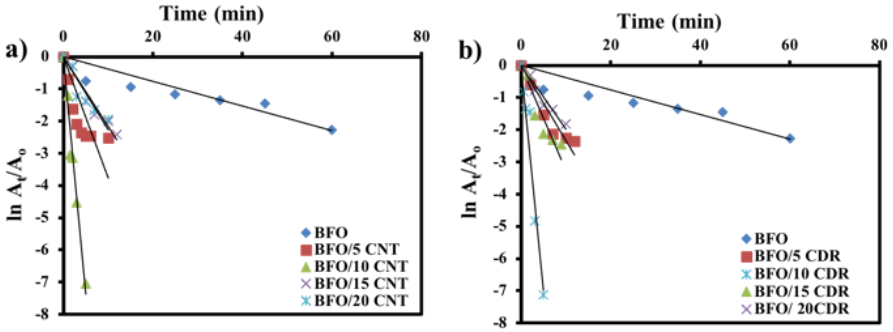

Fig. 15 Pseudo first order kinetic curves for reduction of PNP using (a) BFO/CNT and (b) BFO/CDR nanoparticles

$$\frac{C_e}{q_e} = \frac{1}{Q_m K_L} + C_e/Q_0 \quad (9)$$

$$logq_e = \log K_f + (1/n)\log C_e \quad (10)$$

where K_L represents the Langmuir equilibrium adsorption constant (L mg^{-1}) related to energy of adsorption, q_m is the upper limit monolayer adsorption efficiency of adsorbent, K_F and n are Freundlich constants at constant temperature associated to adsorption capacity and adsorption intensity of adsorbent. Slope and intercept of the linear plot of c_e/q_e *vs.* c_e provides the value of Q_m and K_L as shown in Fig. 12(a) and 13 (a). The values of K_F and 1/n can be computed from intercept and slope of plot of log q_e *vs.* log c_e (Figs. 12(b) and 13(b)). The maximum adsorption capacity of 163.9 mg g^{-1} and 192.9 mg g^{-1} was observed for BFO/20 CNT and BFO/20 CDR, respectively. The values of correlation coefficient (R^2) disclose that the Langmuir equation provides better fit to the given experimental data as that of Freundlich equation. For the Langmuir equation value of the equilibrium parameter R_L (dimensionless factor) was evaluated using equation (Eq. (11)).

$$R_L = 1/(1 + K_L C_0) \quad (11)$$

The value of R_L stipulates the nature of adsorption process, it is favourable if $0 < R_L < 1$, linear when $R_L=1$, unfavourable if $R_L>1$, and for irreversible process $R_L=0$ (Komal *et al*. 2020). The values of dimensionless parameter R_L for the adsorption of MTN were found to be in the range of 0-1, suggesting the favourable adsorption phenomenon. The values of parameters related to Langmuir isotherm are presented in Table 3.

5.3 Adsorption kinetics

The adsorption rate of MTN was investigated using pseudo first order (Eq. (12)) and pseudo second order (Eq. (13)) kinetics equations. The plots of pseudo first order and pseudo second order kinetics of MTN (conc.) adsorption are presented in Figs. 12(c) and (d) and Figs. 13(c) and (d) for BFO/20 CNT and BFO/20 CDR respectively.

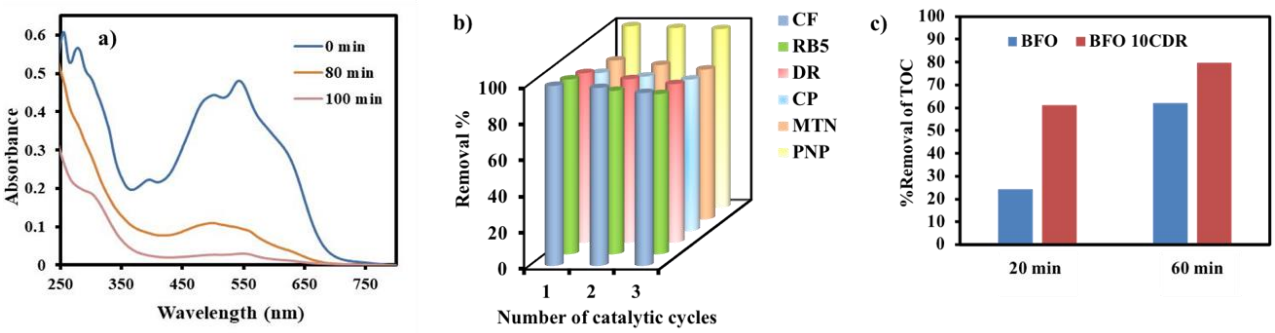

Fig. 16 (a) Time-dependent UV-visible spectra for degradation of RB5, CF, DR and CP in mixture using BFO/10 CDR nanoparticles, (b) recyclability studies of BFO/10 CDR up to 3 catalytic runs and (C) %removal of TOC utilizing BFO and BFO 10CDR nanoparticles (For RB-5 dye)

Table 6 Summary of % Degradation efficiency of BFO/10 CDR

	Removal% (Time in min)		
Pollutants	Single pollutant	In mixture of dyes/drugs	In mixture of dyes and drugs (RB5+CF+DR+CP)
RB5	96.3(20)	94.7 (70) (RB5+CF)	96.9 (100)
CF	99.1(70)	92.0 (70) (RB5+CF)	95.6 (100)
DR	93.3(50)	96.6 (70) (DR+CP)	93.8 (100)
CP	90.5(50)	76.0 (70) (DR+CP)	64.2 (100)

$$log(q_e - q_t) = (log q_e) - (k_1 t)/2.303 \quad (12)$$

$$\frac{t}{q_t} = \left(\frac{1}{k_2 q_e^2}\right) + t/q_e \quad (13)$$

where k_1 and k_2 (min^{-1}) represents the pseudo first order and pseudo second order rate constant, q_e and q_t (mg g^{-1}) denotes the quantity of adsorbent adsorbed on the surface of adsorbate. The value of k_1 and q_e were calculated from the slope and intercept of linear plot between $log(q_e - q_t)$ *vs* t plot and t/q_t *vs* t plot gives the values of k_2 and q_e. The linear plots displaying the pseudo first order and pseudo second order kinetics for MTN adsorption are presented in Figs. 12 and 13, respectively and the values so deduced are mentioned in Table 4. The perceived values of correlation coefficient (R^2) suggest that adsorption phenomena follows pseudo second order kinetics. A high value of regression coefficient i.e., $R^2 > 0.99$ was observed for all the cases.

5.4 Mechanism of adsorption

The plausible mechanism for adsorption of malathion on the surface of BFO/CNT and BFO/CDR is showcased in Fig. 14.

In situ covalent functionalization of CNT and CDR facilitated carboxyl and hydroxyl groups on the surface of nanocomposite, these functional groups entertain the adsorption process by interacting with the pollutant molecules (Dehghani *et al*. 2017). The interactions between malathion and nanocomposite are shown in Fig. 14.

5.5 Regeneration of adsorbent

As adsorption is only a separation process, to avoid environmental contamination (air, water, soil), after extracting the pollutant molecules from the water matrix, the pollutant can be recovered (to reuse) or decomposed as per need. Methods for both the possible treatments are available in reported literature (Massad *et al*. 2021) (Ahmed *et al*. 2012). Before performing re-adsorption studies the adsorbed pollutant molecules were removed from the surface of adsorbent through numerous washings and the regenerated adsorbent was then dried at 70 ºC for 6 h. Regenerated adsorbent was then utilized for further adsorption cycles.

6. Reduction reaction of Para-nitrophenol (PNP)

The use of nitro phenols in industrial and agricultural processes is increasing abruptly and these nitrophenols are extremely toxic, due to their carcinogenic nature. Environmental deterioration due to nitro phenols is at alarming stage, thus their removal from environment is of great need (Goyal *et al*. 2014, Kapoor *et al*. 2020). Adsorption, degradation, and catalytic reduction are various possible ways for removal of nitro phenols. Amongst these, catalytic reduction is a better way, as the reaction byproducts (aminophenols) are less harmful (Gua *et al*. 2016). Moreover, amino phenols can be efficiently utilized in pharmaceutical, dye, paint industries and as lubricating agents in fuels (Shin *et al*. 2012).

6.1 Comparative catalytic behavior of BFO and BFO/ CNT and BFO/CDR nanoparticles for reduction of PNP

The comparative reduction ability of all the synthesized materials was examined using UV–visible spectro-

photometry. The percentage conversion was calculated by using the under given relation (Eq. (14))

$$\%Conversion = \frac{A_0 - A_t}{A_0} * 100 \quad (14)$$

The plots of %conversion *vs.* time for all the synthesized nanomaterials were examined and their correlated parameters are listed in Table 5. It can be clearly observed that amongst all the synthesized nanoparticles BFO/10 CNT and BFO/10 CDR nanoparticles possessed least reaction time for 99.9% and 99.92% conversion, respectively. The results demonstrated that BFO nanoparticles showcased ~ 89% reduction of PNP in 90 min whereas with the addition of 10 wt% of both CNT and CDR, dramatic improvement (99.9% reduction) was observed in just 5 min of reaction time. This dramatic enhancement could be ascribed to the promising modification of BFO nanoparticles with introduction of carbon based materials as a support. Furthermore, introduction of an optimum amount of CNT and CDR resulted in the significant reduction in the reaction time which could be due to enhanced surface area of synthesized nanocomposites.

6.2 Reduction kinetics

The kinetics of reduction reaction was observed to follow pseudo-first-order kinetics with respect to concentration of PNP as $NaBH_4$ was used in abundant amount. The first order rate law equation (Eq. (15)) is given as follow:

$$ln\frac{A_t}{A_0} = -kT \quad (15)$$

The values of rate constant (k) were computed from the slope of linear plot of $\ln(A_t/A_0)$ *vs.* T as depicted in Fig. 15 and their correlated values are listed in Table 5. The observed values of correlation coefficient (R^2) were found extremely close to unity which suggests that pseudo-first-order kinetic model fits well with the experimental data.

6.3 Mechanism of reduction

Addition of $NaBH_4$ in reaction mixture provides Na^+ and BH_4^- ions. With the addition of catalyst, BH_4^- ion and nitrophenol present in reaction mixture immigrate to the surface of the catalyst (BFO). The aqueous medium provides H^+ ions required to accelerate the reduction process. Metal ions present in aqueous solution helps in electron transportation from BH_4^- to PNP, leads to increase in rate of reduction (Wang *et al.* 2019, Goyal *et al.* 2014). The CV studies revealed that both BFO/CNT and BFO/CDR possess higher electron transfer rate as compared to bare BFO and high electron transfer rate leads to higher reduction rate, which is in support with the experimental results. Introduction of carbon based materials proficiently augment the surface area of BFO nanoparticles, which results in large availability of active sites on the surface of nanomaterial. Moreover, the presence of graphitic form of carbon (evidenced from XRD) enhanced the adsorption of PNP over the surface of BFO/CNT and BFO/CDR by π-π stacking interactions (Kapoor *et al.* 2020, Han *et al.* 2019). Hence, hike in surface area, enhanced charge transfer ability, synergistic effect of BFO/CDR and numerous oxygen containing groups of CNT, CDR eventually augmented the electronic and catalytic properties of nanoparticles.

7. Recyclability and reusability

To dissect reusability of synthesized (BFO/10CDR) recyclability and reusability experiments were performed by recovering the catalyst using an external magnet and scrupulously washed with water and ethanol for further use. No appreciable change in activity of nanocatalyst (BFO/10 CDR) was observed up to three cycles for oxidative degradation, adsorption as well as reduction reactions as depicted by bar graphs in Fig. 16 (b). Hence the synthesized BFO/CDR could be utilized for long term prospective implementation.

8. Conclusions

A novel and simplistic assembly of BFO and CDR nanocomposites were prepared utilizing 5, 10, 15 and 20 wt% CDR via simple wet chemical method which exhibits promising photocatalytic, adsorptive as well as reduction properties for environmental remediation.

- The experimental studies bespeaks enrichment in the efficacy of BFO nanoparticles with the introduction of 10 wt% CDR as a beneficial modification, 99.1%, 96.3%, 93.3%, 90.5% degradation was observed for CF, RB5, DR and CP pollutant, respectively.
- Synthesized heterojunction possess excellent efficiency for degradation of mixture of pollutants which makes it potential candidate for practical applicability. The enhancement in surface area with introduction of CDR was observed, and the maximum adsorption capacity for adsorption of pesticide MTN was found to be 192.6 mg g^{-1} for BFO/20CDR.
- This modification was also proved dramatically beneficial for the reduction of PNP, 99.9% conversion of PNP was observed in just 5 min utilizing BFO/10 CDR as catalyst.
- All the results were found comparable with BFO/CNT, hence CDR can be utilized as a better alternative of CNTs for future prospective.

Acknowledgments

The authors are thankful to University Grants Commission (UGC) (Ref no: 27/(CSIR-UGC NET DEC. 2017) (R.No. 107573), and DST/TMD(EWO)/OWUIS-2018/RS-15(G) dated: 15/11/2019 for financial support. The Authors are obliged to Sophisticated Analytical Instrumentation Facility (SAIF), Panjab University, Chandigarh for providing instrumentations facilities.

References

Avilés, F., Cauich-Rodríguez, J.V., Moo-Tah, L. May-Pat, A. and Vargas-Coronado, R. (2009), "Evaluation of mild acid oxidation

treatments for MWCNT functionalization", *Carbon*, **47**, 2970-2975. https://doi.org/10.1016/j.carbon.2009.06.044.

Chatterjee, S., Das, S.K., Chakravarty, R., Chakrabarti, A., Ghosh, S. and Guha, A.K. (2010), "Interaction of malathion, an organophosphorus pesticide with Rhizopus oryzae biomass", *J. Hazard. Mater.*, **174**(1-3), 47–53. https://doi.org/10.1016/j.jhazmat.2009.09.014.

Corbett, J.F. (1972) "Pseudo first-order kinetics", *J. Chem. Educ.*, **49**(10), 663. https://doi.org/10.1021/ed049p663.

Dai, J.F., Xian, T., Di, L.J. and Yang, H. (2013), "Preparation of $BiFeO_3$ -graphene nanocomposites and their enhanced photocatalytic activities", *J. Nanomater.*, **2013**, https://doi.org/10.1155/2013/642897.

Dehghani, M.H., Niasar, Z.S., Mehrnia, M.R., Shayeghi, M., Al-Ghouti, M.A., Heibati, B., McKay, G. and Yetilmezsoy, K. (2017), "Optimizing the removal of organophosphorus pesticide malathion from water using multi-walled carbon nanotubes", *Chem. Eng. J.*, **310**, 22-32. http://doi.org/10.1016/j.cej.2016.10.057.

Delahay, P. (1951), Recent advances in oscillographic polarography", *Anal. Chim. Acta.*, **5**, 129-136. https://doi.org/10.1016/S0003-2670(00)87521-2.

Donia, A.M., Atia, A.A., Hussien, R.A. and Rashad, R.T., (2012), "Comparative study on the adsorption of malathion pesticide by different adsorbents from aqueous solution", *Desalin. Water Treat.*, **47**(1-3), 300-309. https://doi.org/10.1080/19443994.2012.696419.

Ghosh, S., Dasgupta, S., Sen, A. and Sekhar Maiti, H. (2005), "Low-temperature synthesis of nanosized bismuth ferrite by soft chemical route", *J. Am. Ceram. Soc.*, **88**(5), 1349-1352. https://doi.org/10.1111/j.1551-2916.2005.00306.x.

Girgis, E., Adel, D., Tharwat, C., Attallah, O. and Rao, K.V. (2015), "Cobalt ferrite nanotubes and porous nanorods for dye removal", *Adv. Nano Res.*, **3**(2), 111-121 http://doi.org/10.12989/anr.2015.3.2.111.

Goyal, A., Bansal, S. and Singhal, S. (2014), "Facile reduction of nitrophenols: Comparative catalytic efficiency of MFe_2O_4 (M = Ni, Cu, Zn) nano ferrites", *Int. J. Hydrogen Energy.*, **39**(7), 4895-4908. https://doi.org/10.1016/j.ijhydene.2014.01.050.

Guo, P., Tang, L., Tang, J., Zeng, G., Huang, B., Dong, H., Zhang, Y., Zhou, Y., Deng, Y., Ma, L. and Tan, S. (2016), "Catalytic reduction-adsorption for removal of p-nitrophenol and its conversion p-aminophenol from water by gold nanoparticles supported on oxidized mesoporous carbon", *J. Colloid Interf. Sci.*, **469**, 78-85. https://doi.org/10.1016/j.jcis.2016.01.063.

Guo, R., Fang, L., Dong, W., Zheng, F. and Shen, M. (2010), "Enhanced photocatalytic activity and ferromagnetism in Gd doped $BiFeO_3$ nanoparticles", *J. Phys. Chem. C.*, **114**(49), 21390-21396. https://doi.org/10.1021/jp104660a.

Guo, W., Zhang, Z., Lin, H. and Cai, L. (2020), "Z-scheme BiFeO3-CNTs-PPy as a highly effective and stable photo-catalyst for selective oxidation of benzyl alcohol under visible-light irradiation", *Mol. Catal.*, **492**, 111011. https://doi.org/10.1016/j.mcat.2020.111011

Han, F., Xu, X., Fu, Y. and Wang, X. (2019), "Synthesis of rice-husk-carbon-supported nickel ferrite catalyst for reduction of nitrophenols", *J. Nanosci. Nanotechnol.*, **19**(9), 5838-5846. https://doi.org/10.1166/jnn.2019.16567.

Harish, K.N., Bhojya Naik, H.S., Prashanth Kumar, P.N. and Viswanath, R. (2012), "Synthesis, enhanced optical and photocatalytic study of Cd-Zn ferrites under sunlight", *Catal. Sci. Technol.*, **2**, 1033-1039. https://doi.org/10.1039/c2cy00503d.

Hu, Y., Fei, L., Zhang, Y., Yuan, J. Wang, Y. and Gu, H. (2011), "Synthesis of bismuth ferrite nanoparticles via a wet chemical route at low temperature", *J. Nanomater.*, **2011**, https://doi.org/10.1155/2011/797639.

Huang, H.B., Wang, Y., Jiao, W.B., Cai, F.Y. Shen, M., Zhou, S.G., Cao, H.L., Lü J. and R. Cao, (2018), "Lotus-leaf-derived activated-carbon-supported nano-CdS as energy-efficient photo-catalysts under visible irradiation", *ACS Sustain. Chem. Eng.*, **6**(6), 7871-7879. https://doi.org/10.1021/acssuschemeng.8b01021.

Irfan, S., Zhuanghao, Z. Li, F., Chen, Y.X., Liang, G.X. Luo, J.T. and Ping, F. (2019), "Critical review: Bismuth ferrite as an emerging visible light active nanostructured photocatalyst", *J. Mater. Res.*, **8**(6), 6375-6389. https://doi.org/10.1016/j.jmrt.2019.10.004.

Jackson, S.T. and Nuzzo, R.G. (1995), "Determining hybridization differences for amorphous carbon from the XPS C 1s envelope", *Appl. Surf. Sci.*, **90**(2), 195-203. https://doi.org/10.1016/0169-4332(95)00079-8.

Kang, S.T., Seo, J.Y. and. Park, S.H (2015), "The characteristics of CNT/cement composites with acid-treated MWCNTs", *Adv. Mater. Sci. Eng.*, **2015**. http://doi.org/10.1155/2015/308725.

Kapoor, S., Sheoran, A., Riyaz, M. Agarwal, J., Goel, N. and Singhal, S. (2020), "Enhanced catalytic performance of Cu/Cu_2O nanoparticles via introduction of graphene as support for reduction of nitrophenols and ring opening of epoxides with amines established by experimental and theoretical investigations", *J. Catal.*, **381**, 329-346. https://doi.org/10.1016/j.jcat.2019.11.012.

Kaur, J., Gupta, K., Kumar, V., Bansal, S. and Singhal, S. (2016), "Synergic effect of Ag decoration onto ZnO nanoparticles for the remediation of synthetic dye wastewater", *Ceram. Int.*, **42**(2), 2378-2385. https://doi.org/10.1016/j.ceramint.2015.10.035.

Kaur, P., Singh, S., Kumar, V., Tikoo, K.B., Chudasama, B., Kaushik, A. and Singhal, S. (2019), "Interesting makeover of strontium hexaferrites for environment remediation from excellent photocatalysts to outstanding adsorbents via inclusion of Mn^{3+} into the lattice", *J. Alloys Compd.*, **791**, 508-521. https://doi.org/10.1016/j.jallcom.2019.03.312.

Komal, Gupta, K., Kumar, V., Tikoo, K.B., Kaushik, A. and Singhal, S. (2020), "Encrustation of cadmium sulfide nanoparticles into the matrix of biomass derived silanized cellulose nanofibers for adsorptive detoxification of pesticide and textile waste", *Chem. Eng. J.*, **385**, 123700. https://doi.org/10.1016/j.cej.2019.123700.

Lam, S.M., Sin, J.C. and Mohamed, A.R. (2016), "A review on photocatalytic application of g-C_3N_4/semiconductor (CNS) nanocomposites towards the erasure of dyeing wastewater", *Mater. Sci. Semicond. Proc.*, **47**, 62-84. https://doi.org/10.1016/j.mssp.2016.02.019.

Li, T., Shen, J., Li, N. and Ye, M. (2013), "Hydrothermal preparation, characterization and enhanced properties of reduced graphene-$BiFeO_3$ nanocomposite", *Mater. Lett.*, **91**, 42-44. https://doi.org/10.1016/j.matlet.2012.09.045.

Li, Z., Shen, Y., Guan, Y., Hu, Y., Lin, Y. and Nan, C.W. (2014), "Bandgap engineering and enhanced interface coupling of graphene-$BiFeO_3$ nanocomposites as efficient photocatalysts under visible light", *J. Mater. Chem. A.*, **2**(6), 1967-1973. https://doi.org/10.1039/c3ta14269h.

Massad, Y., Hanbali, G., Jodeh, S., Hamed, O., Bzour, M., Dagdag, O. and Samhan, S., (2022), "The efficiency of removal of organophosphorus malathion pesticide using functionalized multi-walled carbon nanotube: Impact of Dissolved Organic Matter (DOM)", Sep. Sci. Technol., 57(1), 1-12. https://doi.org/10.1080/01496395.2021.1881118.

Mukherjee, A., Chakrabarty, S., Kumari, N., Su, W.N. and Basu, S. (2018), "Visible-light-mediated electrocatalytic activity in reduced graphene oxide-supported bismuth ferrite" *Acs Omega*, **3**(6), 946-5957. https://doi.org/10.1021/acsomega.8b00708.

Muller, J., Huaux, F., Moreau, N., Misson, P., Heilier, J.F., Delos,

M., Arras, M., Fonseca, A., Nagy, J.B. and Lison, D. (2005), "Respiratory toxicity of multi-wall carbon nanotubes", *Toxicol. Appl. Pharmacol.*, **207**(14), 221-231. https://doi.org/10.1016/j.taap.2005.01.008.

Niaei, A.H. and Rostamizadeh M. (2020), "Adsorption and electro-Fenton processes over FeZSM-5 nano-zeolite for tetracycline removal from wastewater", *Adv. Nano. Res.*, **9**(3), 173-181. http://doi.org/10.12989/anr.2020.9.3.173.

Noorimotlagh, Z., Kazeminezhad, I., Jaafarzadeh, N., Ahmadi, M., Ramezani, Z. and Martinez, S. (2018), "The visible-light photodegradation of nonylphenol in the presence of carbon-doped TiO_2 with rutile/anatase ratio coated on GAC: Effect of parameters and degradation mechanism", *J. Hazard. Mater.*, **350**, 108-120. https://doi.org/10.1016/j.jhazmat.2018.02.022.

Norizan, M.N., Moklis, M.H., Demon, S.Z.N., Halim, N.A., Samsuri, A., Mohamad, I.S., Knight, V.F. and Abdullah, N. (2020), "Carbon nanotubes: functionalisation and their application in chemical sensors", *RSC Adv.*, **10**(71), 43704-43732. https://doi.org/10.1039/D0RA09438B.

Ortiz-Quiñonez, J.L., Díaz, D., Zumeta-Dubé, I., Arriola-Santamaría, H., Betancourt, I. Santiago-Jacinto, P. and Nava-Etzana, N. (2013), "Easy synthesis of high-purity $BiFeO_3$ nanoparticles: New insights derived from the structural, optical, and magnetic characterization", *Inorg. Chem.*, **52**(18), 10306-10317. https://doi.org/10.1021/ic400627c.

Padmavathy, K.S., Madhu, G. and Haseena P.V. (2016), "A study on effects of pH, adsorbent dosage, time, initial concentration and adsorption isotherm study for the removal of hexavalent chromium (Cr (VI)) from wastewater by magnetite nanoparticles", *Procedia Technol.*, **24**, 585-594. https://doi.org/10.1016/j.protcy.2016.05.127.

Pradeep, A. and Chandrasekaran, G. (2006), "FTIR study of Ni, Cu and Zn substituted nano-particles of $MgFe_2O_4$", *Mater. Lett.*, **60**(3), 371-374. https://doi.org/10.1016/j.matlet.2005.08.053.

Prakash, V., Sharma, S., Kaur, J. and Mehta, S.K. (2018), "Graphene oxide/lysine composite-a potent electron mediator for detection of diazepam", *Anal. Methods.*, **10**(41), 5038-5046. https://doi.org/10.1039/c8ay01429a.

Randles, J.E. (1948), "A cathode ray polarograph. Part II: The current-voltage curves", *Trans. Faraday Soc.*, **44**, 327-338.

Rao, R.A.K. and Kashifuddin, M. (2012), "Adsorption properties of coriander seed powder (Coriandrum sativum): Extraction and pre-concentration of Pb (II), Cu (II) and Zn (II) ions from aqueous solution", *Adsorp. Sci. Technol.*, **30**(2), 127-146. https://doi.org/10.1260/0263-6174.30.2.127.

Ševčík, A. (1948), "Oscillographic polarography with periodical triangular voltage", *Collect. Czechoslov Chem. Commun.*, **13**, 349-377. https://doi.org/10.1135/cccc19480349.

Shah, A.H. and Rather, M.A. (2021), "Pharmaceutical residues: New emerging contaminants and their mitigation by nano-photocatalysis", *Adv. Nano Res.*, **10**(4), 397-414. http://dx.doi.org/10.12989/anr.2021.10.4.397.

Shen, Y., Li, Z., Yang, C., Lei, Y., Guan, Y., Lin, Y., Liu D. and Nan, C.W. (2013), "Significant enhancement in the visible light photocatalytic properties of $BiFeO_3$-graphene nanohybrids", *J. Mater. Chem. A*, **1**(3), 823-829. https://doi.org/10.1039/C2TA00141A.

Shin, K.S., Cho, Y.K., Choi, J.Y. and Kim, K. (2012), "Facile synthesis of silver-deposited silanized magnetite nanoparticles and their application for catalytic reduction of nitrophenols", *Appl. Catal. A Gen.*, **413-414**, 170-175. https://doi.org/10.1016/j.apcata.2011.11.006.

Soleimani, H., Yahya, N., Baig, M.K., Khodapanah, L., Sabet, M., Burda, M., Oechsner, A. and Awang, M. (2015), "Synthesis of carbon nanotubes for oil-water interfacial tension reduction", *Oil Gas Res.*, **1**(1),1000104. https://doi.org/10.4172/2472-0518.1000104.

Soltani, N., Saion, E., Mahmood Mat Yunus, W., Navasery, M., Bahmanrokh, G., Erfani, M., Zare, M.R. and Gharibshahi, E. (2013), "Photocatalytic degradation of methylene blue under visible light using PVP-capped ZnS and CdS nanoparticles", *Sol. Energy.*, **97**, 147-154. https://doi.org/10.1016/j.solener.2013.08.023.

Strømme, M., Niklasson, G.A. and Granqvist, C.G. (1995), "Voltammetry on fractals", *Solid State Commun.*, **96**(3), 151-154. https://doi.org/10.1016/0038-1098(95)00363-0.

Tauc, J., Grigorovici, R. and Vancu, A. (1966), "Optical properties and electronic structure of amorphous germanium", *Phys. Status Solidi B*, **15**(2), 627-637. https://doi.org/10.1002/pssb.19660150224.

Tenorio-González, F.N., Bolarín-Miró, A.M., Sánchez-De Jesús, F., Vera-Serna, P. Menéndez-González, N. and Sánchez-Marcos, J. (2017), "Crystal structure and magnetic properties of high Mn-doped strontium hexaferrite", *J. Alloys Compd.*, **695**, 2083-2090. https://doi.org/10.1016/j.jallcom.2016.11.047.

Tsuboy, M.S., Angeli, J.P.F., Mantovani, M.S., Knasmüller, S., Umbuzeiro, G.A. and Ribeiro, L.R. (2007), "Genotoxic, mutagenic and cytotoxic effects of the commercial dye CI Disperse Blue 291 in the human hepatic cell line HepG2", *Toxicol. Vitr.*, **21**(8),1650-1655. https://doi.org/10.1016/j.tiv.2007.06.020.

Wang, G., Yuan, S., Wu, Z., Liu, W., Zhan, H., Liang, Y., Chen, X., Ma, B. and Bi, S. (2019), "Ultra-low-loading palladium nanoparticles stabilized on nanocrystalline Polyaniline (Pd@ PANI): A efficient, green, and recyclable catalyst for the reduction of nitroarenes", *Appl. Organomet. Chem.*, **33**(11), 5159. https://doi.org/10.1002/aoc.5159.

Wang, X., Fan, J., Qian, F. and Min, Y. (2016), "Magnetic $BiFeO_3$ grafted with MWCNT hybrids as advanced photocatalysts for removing organic contamination with a high concentration", *RSC Adv.*, **6**(55), 49966-49972. https://doi.org/10.1039/c6ra08316a.

CC